Key Points:
- Experimental landslides were smaller than expected and initiated only by near fully saturated conditions, in contrast to model predictions
- Three-dimensional models that include boundary friction can account for heightened stability, but not the observed landslide sizes
- Landslides were thinner and shorter on low-angle hillslopes, with a critical saturation level determined by grain size at the lowest slopes

Correspondence to:
J. P. Prancevic,
jeffrepr@ethz.ch

The Role of Three-Dimensional Boundary Stresses in Limiting the Occurrence and Size of Experimental Landslides

Jeffrey P. Prancevic[1,2] (iD), Michael P. Lamb[1] (iD), Marisa C. Palucis[1,3] (iD), and Jeremy G. Venditti[4] (iD)

[1]Division of Geological and Planetary Sciences, California Institute of Technology, Pasadena, CA, USA, [2]Now at Department of Environmental Systems Science, ETH Zurich, Zurich, Switzerland, [3]Now at Department of Earth Science, Dartmouth College, Hanover, NH, USA, [4]Department of Geography, Simon Fraser University, Burnaby, British Columbia, Canada

Abstract The occurrence of seepage-induced shallow landslides on hillslopes and steep channel beds is important for landscape evolution and natural hazards. Infinite-slope stability models have been applied for seven decades, but sediment beds generally require higher water saturation levels than predicted for failure, and controlled experiments are needed to test models. We initiated 90 landslides in a 5 m long laboratory flume with a range in sediment sizes ($D = 0.7, 2, 5,$ and 15 mm) and hillslope angles ($\theta = 20°$ to 43°), resulting in subsurface flow that spanned the Darcian and turbulent regimes, and failures that occurred with subsaturated and supersaturated sediment beds. Near complete saturation was required for failure in most experiments, with water levels far greater than predicted by infinite-slope stability models. Although 3-D force balance models predict that larger landslides are less stable, observed downslope landslide lengths were typically only several decimeters, not the entire flume length. Boundary stresses associated with short landslides can explain the increased water levels required for failure, and we suggest that short failures are tied to heterogeneities in granular properties. Boundary stresses also limited landslide thicknesses, and landslides progressively thinned on lower gradient hillslopes until they were one grain diameter thick, corresponding to a change from near-saturated to supersaturated sediment beds. Thus, landslides are expected to be thick on steep hillslopes with large frictional stresses acting on the boundaries, whereas landslides should be thin on low-gradient hillslopes or in channel beds with a critical saturation level that is determined by sediment size.

Plain Language Summary Shallow landslides on hillslopes and steep riverbeds commonly occur when rainwater saturates soil enough to outweigh its frictional stability. Landslides play a key role in shaping mountains and pose natural hazards to those living in steep terrain. To predict the occurrence of landslides we often rely on models that have not been verified experimentally. To test these models, we initiated 90 landslides on a laboratory hillslope under a wide range of soil conditions and inclination angles. We found that landslides on very steep hillslopes were nearly as stable as on low gradient hills but were much larger in size. At small hillslope angles, landslides could be as thin as a single sediment grain, and the amount of water required to initiate these slides was determined by sediment size. Landslide models that consider the frictional force acting only at the base of the landslides underpredict stability in all experiments. Frictional forces acting at the boundaries of landslides are often ignored, but including these forces can explain the increased stability of our experimental hillslopes. However, these models are unable to predict the size of the experimental landslides, which were, on average, 10-fold smaller than predicted.

1. Introduction

Mass failure of inclined sediment beds experiencing subsurface flow produces landslides and debris flows that drive landscape evolution (e.g., Stock & Dietrich, 2006) and pose a significant hazard to human life and infrastructure (e.g., Petley, 2012; United States Geological Survey, 2005). Shallow landslides can occur wherever steeply tilted, unlithified sediment beds experience sufficient downslope seepage stress and buoyant forces to become unstable (Haefeli, 1948; Iverson & Major, 1986; Lambe & Whitman, 1969; Skempton & DeLory, 1957; Takahashi, 1978; Taylor, 1948). Consequently, seepage-induced shallow landslides are common on both soil-mantled hillslopes (e.g., Iverson et al., 1997) and steep alluviated channel beds (e.g., Prancevic et al., 2014;

Rickenmann & Zimmermann, 1993,). Once destabilized, landslides can move a short distance before depositing locally or runout downstream as debris flows (e.g., Iverson et al., 1997; Stock & Dietrich, 2006). Regardless of initiation location or runout behavior, the physical processes driving initial failure may be the same (Takahashi, 1978), with the exception that root cohesion is common on vegetated hillslopes and usually absent in channel beds. To predict the occurrence of these events, one-dimensional force balance models have provided a physical basis for understanding the amount of water needed to destabilize soil of a given bulk friction angle, inclination angle, density, cohesion, and porosity (Haefeli, 1948; Lambe & Whitman, 1969; Taylor, 1948). Despite the importance of seepage-induced mass failure and the widespread application of one-dimensional slope stability models in both engineering and geomorphology (e.g., Montgomery & Dietrich, 1994), the most basic version of the model has not been verified with controlled observations.

There are four primary forces typically considered in slope stability analyses: (1) the buoyant weight of sediment under the force of gravity; (2) frictional resistance at the basal and boundary failure planes; (3) seepage stress exerted on sediment grains by water flowing through the subsurface; and (4) cohesion due to root strength, electrostatic forces, or cementation. Aside from cohesion (4), which is difficult to measure (e.g., Schmidt et al., 2001; Waldron & Dakessian, 1981), theory for the remaining forces (1–3) is tractable, enabling the development of force balance models over the past seven decades (Haefeli, 1948; Iverson & Major, 1986; Lambe & Whitman, 1969; Skempton & DeLory, 1957; Taylor, 1948). The simplest form of these models is one dimensional and assumes homogenous conditions (slope, subsurface discharge, soil properties, and soil thickness) infinitely in the cross-slope and along-slope directions. The infinite-slope assumption is never satisfied but is sometimes considered an acceptable approximation when soil thickness is thin relative to the downslope length and cross-slope width (Milledge et al., 2012).

Independent observations of the hydrologic conditions at the time of landsliding are rare, but where available they have shown that the infinite-slope stability model is a poor predictor of landslide conditions (Berti & Simoni, 2005; Montgomery & Dietrich, 1994; Montgomery et al., 2009; Prancevic et al., 2014). In many cases, sediment is observed to be more stable than predicted by slope stability models. For example, in a monitoring effort, Montgomery et al. (2009) found that the infinite-slope model predicted failure to occur in a completely unsaturated state and that root cohesion was needed to explain the observed stability. In their examination of debris flow initiation by failure of a channel bed, Berti and Simoni (2005) found that the infinite-slope model designed for supersaturated conditions (Takahashi, 1978) underpredicted the water discharge required to initiate bed failures by an order of magnitude. In a coarse channel bed, cohesion and root strength are unlikely to account for such a discrepancy. However, subsurface flow through coarse bed sediment may not be Darcian, which violates an assumption of the infinite-slope stability specified by some (e.g., Bear, 1972; Iverson & Major, 1986). Iverson and Major (1986) have also shown theoretically that any model that assumes slope-parallel flow will underestimate the stability of soil if groundwater seepage vectors have a component directed into the sediment bed, as might be the case for soils experiencing infiltration.

On hillslopes that are not sufficiently wide or long, there are additional resisting stresses acting on the lateral and downslope boundaries (or the "walls" and "toe") of the landslide. Although these stresses are generally ignored, several studies have suggested that boundary stresses play a crucial role in the stability of hillslopes (Burroughs, 1984; Dietrich et al., 2007; Milledge et al., 2012; Montgomery et al., 2009, 2014; von Ruette et al., 2013), and in determining both the depth and areal extent of the initial landslide (Bellugi, Milledge, Dietrich, McKean, et al., 2015; Bellugi, Milledge, Dietrich, Perron, et al., 2015; Dietrich et al., 2007; Milledge et al., 2014). By setting the initial landslide size, boundary stresses might be critically important in determining landslide risk and geomorphic impact (von Ruette et al., 2016). In order to assess the validity of three-dimensional models versus simpler, more commonly applied infinite-slope models, we require controlled observations of slope stability in the absence of other confounding factors.

Laboratory flume experiments provide a controlled setting to test slope stability models, but few have been performed. In some experiments, landslides have been initiated by exfiltrating water from a cut-slope geometry and do not provide a test of the infinite-slope geometry (Eckersley, 1990; Wang & Sassa, 2003). In other experiments, researchers have rained on laboratory hillslopes for the purposes of measuring pore pressure responses during the onset of failure (Iverson et al., 2000; Moriwaki, 1993; Moriwaki et al., 2004; Okura et al., 2002; Reid et al., 1997; Wang & Sassa, 2003; Yagi & Yatabe, 1987). These studies are useful for understanding how sediment is fluidized once ruptured, but the overhead application and infiltration of rainfall complicates the comparison against the infinite-slope stability model, which assumes uniform slope-parallel seepage.

Prancevic et al. (2014) observed heightened sediment bed stability in a laboratory flume that lacked cohesion, roots, or stabilizing seepage flow paths. However, their study was limited to relatively low bed angles ($\theta \leq 33.0°$, where θ is the bed slope angle) and utilized only coarse-grained sediment ($D = 15$ mm, where D is median grain diameter). In their experiments, the channel bed destabilized only when surface flow was present, resulting in shallow landslides of a limited number of grains. They found that the infinite-slope stability model underpredicted the degree of saturation needed to initiate failure, which they attributed to a heightened friction angle associated with small landslide sizes relative to the particle size. However, their experiments also had turbulent subsurface flow, which may have had an additional stabilizing effect (Prancevic et al., 2014).

In this study we performed a series of laboratory flume experiments with a range of hillslope angles, grain sizes, and sediment bed thicknesses to test the infinite-slope stability model and assess potential stabilizing mechanisms. We conducted five sets of experiments with each set corresponding to a particular grain size and sediment bed thickness. Each set was conducted over a wide range of hillslope angles. Grain size was varied in order to test for the effect of turbulence in reducing subsurface flow velocities and stabilizing the sediment. We compare the results of these experiments to an infinite-slope stability model and to a model that considers frictional stresses at the edges of the landslides.

In the following sections, we first review the derivations of both the 1-D (infinite slope) and 3-D (finite width and length) slope stability models (section 2). We then describe our experimental procedure (section 3) before presenting our experimental observations and comparing our observations to model predictions (section 4). Finally, we discuss the validity and application of the 3-D slope stability model for predicting landscape evolution and natural hazards (section 5).

2. Model for Slope Stability

2.1. Infinite-Slope Stability Model

The original one-dimensional slope stability models, proposed first by Taylor (1948) and Haefeli (1948), have served as the basis for subsequent models that incorporate a variety of effects from cohesion, wall friction (e.g., Lambe & Whitman, 1969), nonparallel seepage vectors (Iverson & Major, 1986), partially saturated conditions (Lu & Godt, 2008), and so forth. The model begins with a Mohr-Coulomb failure criteria:

$$\tau = \sigma \tan \phi_b \tag{1}$$

where τ is shear stress acting on the failure plane, σ is the normal stress acting on the failure plane, and ϕ_b is the friction angle of the failure plane. Two alternative parameterizations of τ and σ have been proposed: one that considers the Coulomb friction of only the solid phase with buoyant and seepage forces acting on that solid phase and another that considers the Coulomb friction model of the wet bulk material with basal pore pressure (u) reducing the effective normal stress, (i.e., $\overline{\sigma} = \sigma - u$). These two derivations have previously been shown to be equivalent (e.g., Lambe & Whitman, 1969).

Here we derive the Mohr-Coulomb stress balance in the parameterization that considers seepage and buoyant forces acting only on the solid phase following Lambe and Whitman (1969). In this one-dimensional model, a soil layer of thickness, Z, is saturated to some water level, H, measured in the surface-normal direction relative to the sediment-bedrock interface (Figures 1a and 1b). For simplicity, we assume that there is no zone of partial saturation above $z = H$. The inclination angle, θ, is assumed to be the same for the bedrock, soil, and water surfaces, and seepage is directed parallel to these surfaces. If the driving shear stresses are higher than the resisting stresses for some portion of the soil depth, then that portion of the sediment bed is predicted to fail and slide downslope. The failure plane is defined as the surface where the driving stresses are exactly equal to the resisting stresses at some distance from the sediment base, z_f. Consequently, it is useful to define a water flow thickness, $h = H - z_f$, and failure plane depth, $z_t = Z - z_f$, measured relative to the failure plane (Figures 1a and 1b).

On hillslopes that are sufficiently steep, it is expected that failure will occur under subsaturated conditions (i.e., $h_c < z_t$; Figure 1a). To solve for the conditions at failure, the unit buoyant weight of the sediment grains above the failure plane, γ_b, can be defined as

$$\gamma_{b,\text{sub}} = \left(\rho_s - \rho_f \frac{h}{z_t} \right)(1 - \eta)g \tag{2}$$

Infinite slope schematics
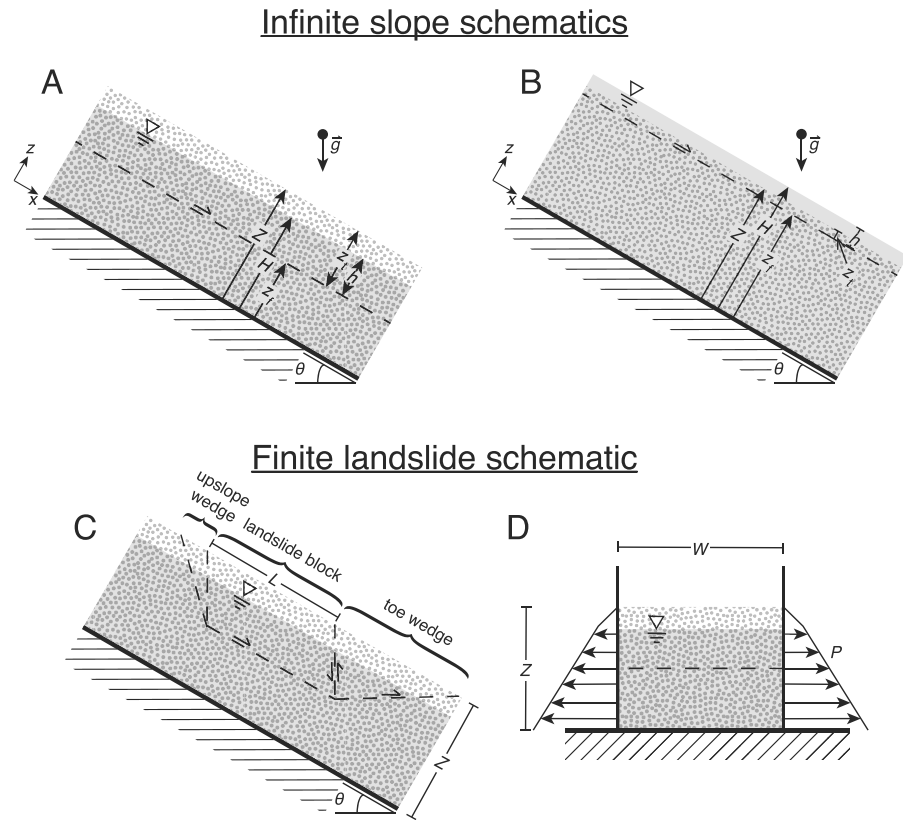

Finite landslide schematic

Figure 1. Schematics of sediment beds at the initiation of a landslide. Dashed lines indicate planes of relative motion and frictional resistance. Two slopes that are assumed to extend infinitely in the along-slope and cross-slope directions and are undergoing failure with (a) only subsurface seepage flow and with (b) surface and subsurface flow. The following symbols are shown: total bed thickness, Z; total water depth (subsurface and surface), H; the distance from the sediment base to the failure plane, z_f; the thickness of the failure, z_t; and the water depth above the failure plane, h. θ is the inclination angle of the bed. A landslide with finite length and width from (c) a cross-slope perspective and (d) an along-slope perspective looking in the downslope direction. This landslide is broken into three sections: the landslide block has an initial direction of motion that is directly downslope, the toe wedge has a component of motion toward the surface of the sediment bed, and the upslope wedge pushes downward on the landslide block. The arrows originating at the sides of the landslide (Figure 1d) indicate the expected distribution of Earth pressure, P.

where g is gravitational acceleration, ρ_s is the material density of the sediment grains, ρ_f is the fluid material density, and η is the porosity.

Following Lambe and Whitman (1969), we use the buoyant unit weight of the soil to compute the normal stress that is exerted by a unit column of sediment of depth z_t on the failure plane as (Figures 1a and 1b):

$$\sigma = z_t \gamma_b \cos \theta. \tag{3}$$

The shear stress exerted by the sediment and water on the failure plane, when averaged over the unit volume of soil, is composed of the downslope component of the buoyant unit weight of the soil, and also the seepage stress exerted by the fluid on the grains:

$$\tau = \underbrace{z_t \gamma_b \sin \theta}_{\text{buoyant sediment stress}} + \underbrace{h \rho_f g \sin \theta}_{\text{seepage stress}} \tag{4}$$

where the seepage stress is calculated as the gravitational head loss of the fluid integrated across the sediment column. In order for equation (4) to be valid, the fluid must not be accelerating, on average, so that the spatial gradient in hydraulic head is balanced by the downslope-oriented seepage stress.

Failure is predicted to occur when the control volume satisfies the Mohr-Coloumb failure criteria (equation (1)). Substituting equations (3) and (4) into equation (1) and setting $\gamma_b = \gamma_{b,\text{sub}}$ yields

$$\frac{h_c}{z_t} = \frac{\rho_s}{\rho_f} \frac{\frac{\tan \phi_b}{\tan \theta} - 1}{\frac{\eta}{1-\eta} + \frac{\tan \phi_b}{\tan \theta}}. \tag{5}$$

In addition to Lambe and Whitman (1969), equation (5) is the critical saturation predicted to produce failure in most previous derivations of infinite-slope stability (Haefeli, 1948; Iverson & Major, 1986; Skempton & DeLory, 1957; Taylor, 1948).

Lu and Likos (2004) showed the potential for suction stress to exert an additional stabilizing stress on the sediment bed that is absent in the typical infinite-slope stability model (equation (5)), particularly in fine-grained soils (sands and finer). However, we do not consider suction stresses in our model because the basal failure planes in our experiments were always located within the fully saturated zone where these stresses are absent. Suction stresses likely were acting on the unsaturated portion of the failure plane (walls and toe), but following Lu and Godt (2008), we estimate suction stresses to be orders of magnitude smaller than the total frictional stresses.

2.1.1. Supersaturated Failures

On hillslopes that are sufficiently low sloping, equation (5) will yield a critical flow depth that is predicted to be greater than the soil thickness ($\frac{h_c}{z_t} \geq 1$; Figure 1c) and equation (5) is no longer applicable. In this case, the unit weight of the buoyant sediment must be modified to limit the magnitude of the buoyant force acting on the grains within the supersaturated regime:

$$\gamma_{b,\text{surf}} = (\rho_s - \rho_f)(1 - \eta)g. \tag{6}$$

By setting the buoyant sediment weight in equations (3) and (4) to this value ($\gamma_b = \gamma_{b,\text{surf}}$), we solve for the critical flow depth in the supersaturated regime:

$$\frac{h_c}{z_t} = \frac{\rho_s - \rho_f}{\rho_f}(1 - \eta)\left(\frac{\tan \phi_b}{\tan \theta} - 1\right) \tag{7}$$

which is the equation first derived by Takahashi (1978).

2.1.2. Failure Plane Depth

Failure plane depth, z_t, is not explicitly defined in equations (5) and (7) but can be predicted by the calculated stress distributions with depth. For the case of subsaturated failure ($H_c < Z$), the deepest failure plane always experiences the highest saturation level (i.e., the maximum value of h_c/z_t is H_c/Z), and is therefore expected to fail most readily (Takahashi, 1978). In contrast, for the case of supersaturated soil ($H_c > Z$), dilute surface flow concentrates stress at the surface of the sediment bed. In this case the preferred failure plane is expected to abruptly shift to the shallowest possible soil depth, which is equal to the diameter of a single grain ($z_t = D$) (Takahashi, 1978; Prancevic et al., 2014).

2.2. Boundary Stresses

When a hillslope is not infinitely wide or long, then some of the frictional resistance to failure occurs at the lateral and downslope boundaries of the landslide, where the slip surface returns to the soil surface (e.g., Bellugi, Milledge, Dietrich, McKean, et al., 2015; Lambe & Whitman, 1969; Milledge et al., 2014; Montgomery et al., 2009). There is an infinite number of possible landslide geometries, and methods exist to numerically solve the 3-D force balance for arbitrary geometries (e.g., Reid et al., 2015; Stark & Eid, 1998). Here we consider a simple landslide geometry composed of a prismatic landslide block with vertical sides and bound by wedges at the upstream and downstream boundaries (Figures 1c and 1d). The downslope wedge exerts resisting stresses in the form of friction along the base of the wedge (on the failure plane) and friction between the wedge and the upslope slab, which are mobilized with different trajectories. At the lateral boundaries, the sides of the mobile block must slide against the walls of the failure scarp. In order to overcome the additional resisting stresses, an increased saturation level is required to initiate failure.

Following Milledge et al. (2014) and Bellugi, Milledge, Dietrich, McKean, et al. (2015), the depth-integrated wall, τ_w, and toe, τ_t, resistance in subsaturated conditions $\left(\frac{h_c}{z_t} \leq 1\right)$ can be estimated using the following respective relationships:

$$\tau_{w,\text{sub}} = \frac{1}{2}K_0 z_t \left(\rho_s - \frac{h^2}{z_t^2}\rho_f\right)(1 - \eta)g \tan \phi_w \tag{8}$$

$$\tau_{t,\text{sub}} = \frac{1}{2} K_P z_t \left(\rho_s - \frac{h^2}{z_t^2} \rho_f \right) (1 - \eta) g (\cos(\phi_b - \theta) - \sin(\phi_b - \theta) \tan \phi_b) \tag{9}$$

where $\tan \phi_w$ is the frictional coefficient between the sediment grains and flume walls, and K_0 and K_P are nondimensional coefficients relating the weight of overbearing sediment to the earth pressure exerted on the walls and toe, respectively. The most commonly used earth pressure coefficient for wall stress is based on an empirical study by Jaky (1944):

$$K_0 = (1 - \sin \phi_b). \tag{10}$$

Several theoretical formulations of the toe (or "passive") earth pressure coefficient have been proposed (see discussion in Milledge et al., 2014). For this study, we employ the Coulomb passive earth pressure coefficient because it is a conservative upper bound and is explicitly defined as

$$K_P = \left(1 - \sqrt{\frac{\sin(2\phi_b) \sin(\phi_b - \theta)}{\cos \phi_b \cos(-\theta)}} \right)^{-2} \cos \phi_b. \tag{11}$$

Finite landslide geometries are also subjected to a destabilizing force from the weight of the upslope wedge that is partially supported by the failed mass, τ_u (Figure 1c). At hillslope angles lower than the bulk friction angle, the magnitude of this additional driving stress is typically orders-of-magnitude smaller than the resisting toe stress, but these stresses become similar in magnitude at hillslope angles that approach the bulk friction angle. In subsaturated conditions τ_u is defined as

$$\tau_{u,\text{sub}} = \frac{1}{2} K_A z_t \left(\rho_s - \frac{h^2}{z_t^2} \rho_f \right) (1 - \eta) g (\cos(\phi_b - \theta) - \sin(\phi_b - \theta) \tan \phi_b) \tag{12}$$

where K_A is the Coulomb active earth pressure coefficient:

$$K_A = \left(1 + \sqrt{\frac{\sin(2\phi_b) \sin(\phi_b - \theta)}{\cos \phi_b \cos \theta}} \right)^{-2} \cos \phi_b. \tag{13}$$

In order to combine all stresses into the Mohr-Coulomb stress balance (equation (1)), the stresses must be integrated and normalized over their relevant surface areas. Adding the toe and wall stress terms to equation (1), multiplying the stresses by their relevant surface areas, and normalizing by LWz_t yields the following Mohr-Coulomb force balance:

$$\underbrace{\gamma_b \sin \theta}_{\substack{\text{buoyant} \\ \text{sediment weight}}} + \underbrace{\frac{h}{z_t} \rho_f g \sin \theta}_{\substack{\text{seepage} \\ \text{stress}}} + \underbrace{\frac{\tau_u}{L}}_{\substack{\text{upslope} \\ \text{wedge} \\ \text{weight}}} = \underbrace{\gamma_b \cos \theta \tan \phi_b}_{\text{basal friction}} + \underbrace{2 \frac{\tau_w}{W}}_{\substack{\text{wall} \\ \text{friction}}} + \underbrace{\frac{\tau_t}{L}}_{\substack{\text{toe} \\ \text{friction}}}. \tag{14}$$

We now substitute the relevant expressions for $\gamma_b = \gamma_{b,\text{sub}}$, $\tau_w = \tau_{w,\text{sub}}$, $\tau_u = \tau_{u,\text{sub}}$, and $\tau_t = \tau_{t,\text{sub}}$ into equation (14) and rearrange to calculate the critical flow depth:

$$\frac{h_c}{z_t} = \frac{-S_3 + \left[S_3^2 - 4 \frac{\rho_s}{\rho_f} \frac{z_t}{W} S_1 \left(S_2 - \frac{z_t}{W} S_1 \right) \right]^{1/2}}{2 \frac{z_t}{W} S_1}, \tag{15}$$

in which

$$S_1 = K_0 \tan \phi_w + \frac{W}{2L} (\cos(\phi_b - \theta) - \sin(\phi_b - \theta) \tan \phi_b)(K_P - K_A) \tag{16}$$

$$S_2 = \sin \theta - \cos \theta \tan \phi_b \tag{17}$$

$$S_3 = \frac{\eta}{1 - \eta} \sin \theta + \cos \theta \tan \phi_b. \tag{18}$$

2.2.1. Supersaturated Failures With Boundary Stresses

Boundary stresses in the supersaturated regime are expected to be considerably smaller due to the relatively shallow failure plane depths. We solve for a slightly higher critical flow depth for failure by calculating new expressions for boundary stresses for the supersaturated regime. The expressions for $\tau_{w,\text{surf}}$, $\tau_{t,\text{surf}}$, and $\tau_{u,\text{surf}}$ differ from $\tau_{w,\text{sub}}$, $\tau_{t,\text{sub}}$, and $\tau_{u,\text{sub}}$ (equations (8), (9), and (12)) only in that we set $\frac{h^2}{z_t^2} = 1$ to limit the buoyant force to the sediment column. Substituting the definitions of $\gamma_b = \gamma_{b,\text{surf}}$, $\tau_w = \tau_{w,\text{surf}}$, $\tau_t = \tau_{t,\text{surf}}$, and $\tau_u = \tau_{u,\text{surf}}$ into equation (14) and solving for $\frac{h_c}{z_t}$ yields

$$\frac{h_c}{z_t} = \frac{\rho_s - \rho_f}{\rho_f}(1 - \eta)\left(\frac{\tan\phi_b}{\tan\theta} + \frac{z_t}{W}\frac{S_1}{\sin\theta} - 1\right).$$

(19)

2.2.2. Failure Plane Depth With Boundary Stresses

Solving equations (15) and (19) for the critical water depth (h_c) requires that the failure plane depth (z_t) is known. In addition, z_t is predicted to vary with the surface area of the landslide (L and W). Inspection of equations (15) and (19) reveals that the critical saturation level for failure $\left(\frac{h_c}{z_t}\right)$ decreases as the width, W, and length, L, of the failure increase. This indicates that, in both supersaturated and subsaturated cases, larger landslides are less stable than smaller ones, because the proportion of frictional resistance exerted by the boundaries is smaller. The same finding is true of more complicated numerical predictions that use the Ordinary or Bishop's methods of slices (e.g., Reid et al., 2015). Consequently, the expected landslide surface area for our experiments is defined by the dimensions of the experimental test section: $L = 4$ m and $W = 9.7$ cm (see section 3).

In terms of landslide thickness, z_t, with surface flow present (equation (19)), the shallowest possible failure plane (a single grain layer) will be favored because of the high ratio of driving stress to resisting stress at the bed surface. This is the same depth predicted by the infinite-slope model (section 2.1.2). However, failures occurring under subsaturated conditions will not necessarily rupture at the deepest possible failure plane, as predicted by the infinite-slope model. Although the saturation value is highest at the base of the sediment bed ($[h_c/z_t]_{\max} = H_c/Z$), the total resisting force exerted by the boundaries increases quadratically with depth. The most susceptible failure plane is therefore determined by a competition between linearly increasing driving stress and a quadratically increasing resisting stress with depth. We solve for the weakest failure plane ($z_{t,c}$) by substituting $h_c = H_c - Z + z_t$ into equation (15) and finding the minimum flow depth required to initiate failure (H_c). Differentiating equation (15) with respect to z_t, setting $\frac{dH_c}{dz_t} = 0$, and solving for $z_{t,c}$ gives the preferred failure plane depth:

$$z_{t,c} = \frac{WS_2}{2S_1}\left(1 - \sqrt{1 - \frac{\frac{\rho_s}{\rho_f} - \frac{\rho_f S_3^2}{\rho_s S_2^2}}{\frac{\rho_s}{\rho_f} - 1}}\right).$$

(20)

Note that there are physical limits to $z_{t,c}$ that are not predicted by equation (20). The landslide cannot be thicker than the total bed thickness, Z, and it cannot be thinner than the diameter of a single grain, D (Takahashi, 1978). If the predicted failure plane depth is outside those physical bounds, then we set the failure plane depth equal to the bounding value.

3. Experimental Procedure

To test the validity of equations (7), (5), (15), and (19), we initiated 90 landslides under 24 different experimental conditions at the Caltech Earth Surface Dynamics Laboratory (Figure 2a). Our goal was to conduct experiments with a long section of uniform conditions to best approximate a one-dimensional stress state (e.g., Figures 1a and 1b). In order to accomplish this, our experimental test section was 5 m in length with smooth vertical walls spaced 9.7 cm apart. The middle 4 m of the test section contained a bed of uniform-sized, natural sediment with a constant bed thickness, providing a bed surface that was parallel to the floor of the flume (Figure 2a). The entire test section could be tilted over a wide range of hillslope angles (Figure 2a). Water was introduced at the upstream inlet to the test section and was drained at the downstream outlet of the flume, providing a uniform discharge throughout the length of the flume. The downstream boundary of the test section was a fixed mesh that allowed water to drain and provided a buttress for the granular material.
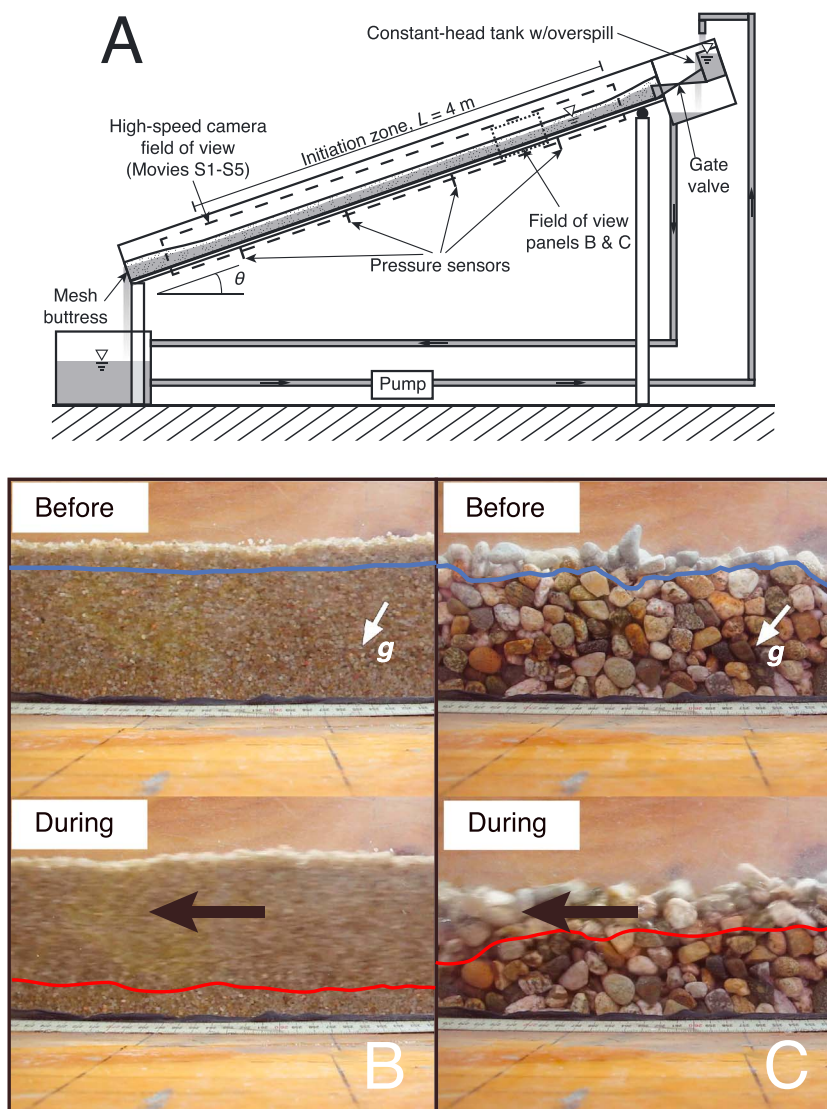
Figure 2. (a) Schematic of the experimental flume, and photos of experimental landslides using (b) 2 mm sand and (c) 15 mm gravel. The flume was tilted to $\theta = 34.5°$ and $41.2°$ in Figures 2b and 2c, respectively, and the photographs were captured with the camera mounted parallel with the flume floor. A gravity vector in each panel shows the vertical downward direction. The top half of each panel shows the sediment bed prior to failure. The bottom half shows the bed during the first seconds of a landslide. The motion blur of the lower panels provides a visualization of the depth of the failure plane in those experiments. Black arrows indicate the direction of motion, the blue lines indicate the water surfaces prior to failure, and the red lines indicate the location of the failure plane at the time of the photograph.

The buttress forced the toe wedge of the landslide (e.g., Figure 1c) to be located somewhere upstream of the outlet of the test section. The basal boundary condition of the experiments was a single layer of glued sediment grains that prevented sliding of the sediment along the otherwise smooth flume floor. The size of the glued grains matched the size of the loose sediment of a given experiment set. The upstream and downstream boundary conditions were 0.5 m long sections with a thicker sediment bed (Figure 2a), ensuring lower H/Z values at the boundaries, and encouraging failure to occur away from the boundaries. We used two materials for the flume walls: the right wall was wooden with a smooth epoxy surface, while the left wall was a clear acrylic plate that allowed us to view the hydraulic conditions within the pore space and document deformation of the sediment bed. The relatively narrow flume width that we used was chosen to reduce lateral variability in hydraulic flow conditions and granular behavior, such that we assume the conditions observed through the acrylic wall were representative of the entire flume width.

Table 1
Experiment Sets

Experimental set	Material	Slope range, θ (deg)	Number of failures	Experimental bed thickness, Z (cm)	Average subsurface flow Reynolds number, $\overline{Re}$
1	Coarse sand	23.9 to 38.0	29	6	1.94
2	Granules	23.9 to 36.5	31	8	28.1
3	Fine gravel	19.6 to 39.2	14	18	181
4	Coarse gravel	33.1 to 43.1	14	10	1,040
5	Coarse gravel	41.2	2	19.5	1,115
Prancevic et al. (2014)	Coarse gravel	25.2 to 33.0	8	10	921

We conducted a total of five experiment sets (Table 1). Each experiment set used a different combination of sediment size (D) and bed thickness (Z). Within each experiment set, we varied hillslope angle as the independent variable and measured the flow depth required to initiate a landslide at that hillslope angle. In the supersaturated failure regime, the surface flow depths that cause failure are similar to a single grain diameter (Prancevic et al., 2014). For experiments with sand and granule beds, resolving changes in such small flow depths was not possible, so we did not conduct experiments within the supersaturated failure regime for those grain sizes. For the 5 mm gravel (set 3), we probed the supersaturated regime, and for the 15 mm gravel we compare our experiments against the supersaturated failure data from Prancevic et al. (2014). Hillslope angles were measured with respect to gravity using the vertical heights of the test section at the upstream and downstream ends (Figure 2a) with an accuracy of $\pm 0.06°$. We conducted multiple experiments at each hillslope angle, and all reported values of saturation level and failure plane depth are averages of repeat experiments.

To test for the effects of non-Darcian subsurface flow, Experiment Sets 1 through 4 each used a unique size of well-sorted sediment: $D = 0.7, 2.0, 5, 15$ mm, respectively (Table 1). Grain sizes were chosen to span Darcian ($Re < 10^1$) to turbulent ($Re > 10^2$) flow regimes according to Reynolds numbers:

$$Re = \frac{qD}{v}, \tag{21}$$

where v is kinematic viscosity and $q = $ (pore fluid velocity $\times$ porosity) is the specific discharge of the pore fluid (e.g., Bear, 1972; Zeng & Grigg, 2006). All of the sediment tested consisted of natural, subrounded silicate grains. Both the coarse sand and the granule materials had high sphericity, while both gravel sizes were more prolate (rod shaped).

For each grain size we measured the material density (ρ_s), bulk porosity (η), dry bulk friction angle (ϕ_b), and the static coefficient of friction between the bulk material and the flume sidewalls (ϕ_w) (Table 2). Density was calculated by measuring displaced water volume in a graduated cylinder and the associated sediment mass with a balance. Bulk porosity was measured by filling a bucket with sediment and measuring the increased mass associated with filling the pore space with water. Dry bulk friction angle was measured by placing a 10 cm thick bed of dry sediment in a 1 m long, 13 cm wide box and then tilting the entire box until a dry granular avalanche was initiated (following Carson, 1977 and Iverson et al., 2004). The inclination angle at the time

Table 2
Sediment Properties

Material	Median grain size, D (mm)	Material density, ρ_s (g/cm^3)	Porosity, η	Bulk friction angle, ϕ_b (deg)	Friction angle with wall, ϕ_w (deg)
Coarse sand	0.7	2.7	0.42	38.3 ± 0.7	28.2
Granules	2	2.69	0.39	38.7 ± 1.0	15.4
Fine gravel	5	2.65	0.43	40.9 ± 0.6	16.7
Coarse gravel	15	2.65	0.43	45.1 ± 1.6	15.2

of avalanche is predicted to be slightly higher than the dry bulk friction angle of the sediment due to a small component of wall friction. By assuming that dry avalanches started at the surface grain layer, which is consistent with our visual observations and theoretically most favorable, the measured bulk friction angle, $\phi_{b,meas}$, was corrected for these small wall effects: $\tan \phi_b = \tan \phi_{b,meas} - K_0 \frac{D}{W} \frac{\tan \phi_w}{\cos \phi_b}$. Similarly, the friction angle associated with wall stress (ϕ_w) was measured by gluing the sediment to blocks of wood (20 cm long by 10 cm wide) and measuring the sliding angle of those blocks on a smooth acrylic surface. Each of these measurements was repeated at least 15 times in order to characterize variability, and we use the mean values in our analysis (Table 2).

Each run within an experiment set began with the same initial surface-normal sediment bed thickness, ranging from $Z = 6$ to 19.5 cm for different experiment sets (Table 1). To test for any effects on slope stability due to bed thickness relative to grain size (Z/D), Experiment Set 5 used the same sediment as set 4 ($D = 15$ mm) but with a thicker sediment bed: $Z = 19.5$ cm versus 10 cm. Bed thicknesses were measured visually using four rulers spaced at 1 m intervals and mounted orthogonal to the flume floor. The bed surface was graded by hand evenly between these measurement locations to achieve a constant bed thickness.

After the test section was prepared (hillslope angle set and sediment graded), experiments proceeded by incrementally increasing the discharge flowing into the top of the test section until the conditions for failure were reached. For all experiments, increments of increased discharge were limited to 10% of the preceding discharge. At each new discharge, the flow was allowed to achieve a steady and uniform depth throughout the entire length of the test section before measurements were made. The steady state condition was determined by continuously monitoring pore pressure readings from four basal pore pressure sensors located 1, 2, 3, and 4 m from the inlet of the test section (Figure 2a), and the time required to achieve steady state ranged from 15 s for the coarse gravel to 720 s for the coarse sand. All pressure sensors were gauge sensors (pressure measured relative to atmospheric) made by Omega (PX409) and were calibrated to 1 mm accuracy in hydraulic head.

Once a steady and uniform flow was achieved, we measured flow discharge by collecting water at the outlet of the flume over a known time interval and weighing it. For most experiments we recorded water level using two methods: (1) by making visual observations of pore saturation once per each stable discharge at 1 mm resolution, and (2) continuously using the pressure sensors. Partial saturation in the coarse sand prohibited the visual estimation of saturated depth, and we rely only on pressure measurements for Experiment Set 1. Flow depths were calculated from the pressure sensors by assuming a parallel-flow pressure distribution: $H = P/(\rho_w g \cos \theta)$, where P is measured pressure (Chaudhry, 2008, p. 18). We used the mean of the four pressure measurements along the length of our flume to calculate flow depths within 1 s of each failure, $H_{c,P}$. For each experiment, we characterized error in pressure-derived flow depths as the standard error between the four sensors at the time of failure. If the standard deviation of critical flow depths between repeat experiments with the same experimental condition was larger than the standard error associated with the pressure measurements, then this standard deviation is reported as the error bars (Figure 3). We also report the averages of our visual estimates of flow depth, $H_{c,V}$, along with error bars from repeat experiments. We utilized a Phantom high-speed camera to record each experimental landslide. The camera captured the entire 4 m planar section of the flume with frame rates up to 250 fps. The camera was synchronized with the pressure sensors to precisely record the timing of failure. For each failure, we also used the high-speed camera to measure the maximum depth and length of grain displacement in the first few video frames during landslide initiation. Initial failure plane depths, z_t, and lengths, L, varied substantially, and we report the average and standard deviations of repeat experiments for each experimental condition (Figures 3 and 4 and Table S1 in the supporting information).

4. Experimental Results

4.1. Landslide Characteristics

All experimental conditions exhibited en masse failure of the sediment bed, where a collection of hundreds to thousands of grains began moving in the downslope direction (Movies S1 to S5 in the supporting information). The sizes of the landslides varied, but the configuration of the failure plane was generally consistent with our model setup: a prismatic landslide moved in the downslope direction, and sediment at the upslope and downslope boundaries had velocity components directed toward and away from the sediment bed, respectively. Landslide behavior varied between experiments of different grain size. Beds composed of the
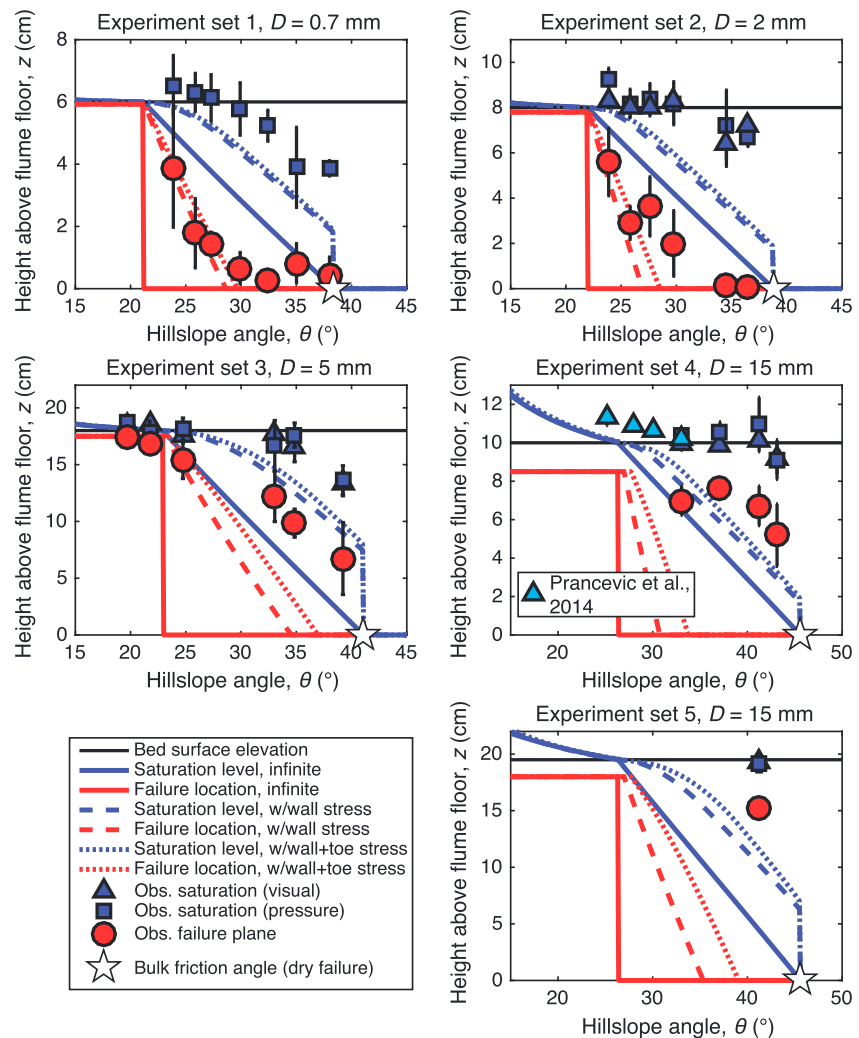
Figure 3. The critical flow depth required to initiate failure and the initial failure plane depth as a function of hillslope angle for all five experiment sets. The base of the sediment bed (flume floor) is located at $z = 0$ cm. The horizontal black line indicates the bed surface for each experiment set. The data points correspond to paired experimental observations of critical flow depth (blue squares and triangles) and initial failure plane depth (red circles). The error bars represent either the standard deviation between repeat experiments at the same hillslope angle (failure plane depths and saturation levels) or the standard error of the four basal pore pressure measurements at the time of failure, if larger. Three model predictions are shown for each experiment set: the stability of an infinite slope (solid lines), the stability of a slope with finite width and wall stress (dashed lines, $W = 9.7$ cm), and the stability of a slope with finite width and length (dotted lines, $W = 9.7$ cm and $L = 4$ m). Paired predictions are shown for each model output of both the failure plane location (red lines) and critical saturation level (blue lines).

finest material ($D = 0.7$ mm) rarely exhibited catastrophic landslides and instead failed as slumps that moved downslope slowly (less than 1 mm/s), sometimes stalling after moving only several centimeters (Movie S1). These slumps often left ~1 cm high headscarps that were supported by suction stress near the bed surface (Figure 2b). In many experiments, the granule material ($D = 2$ mm) also exhibited slow-moving slides that continued downslope in pulses, although an apparent lack of suction stress near the surface prevented the formation of headscarps (Movie S2). At the steepest slopes tested with the granule material, landslides rapidly accelerated downslope (up to 1 m/s), evacuating the entire sediment bed (Figure 2c and Movie S3). The beds of gravel ($D = 5$ and 15 mm) primarily failed in this catastrophic fashion, and high-speed video was required to visualize the rapid deformation of the sediment bed (Figure 2c and Movies S4 and S5). The gravel experiments also had a failure with plane depth, z_t, that was closer to the bed surface than the sand and granule experiments (Figure 2c), which will be discussed in section 4.3.
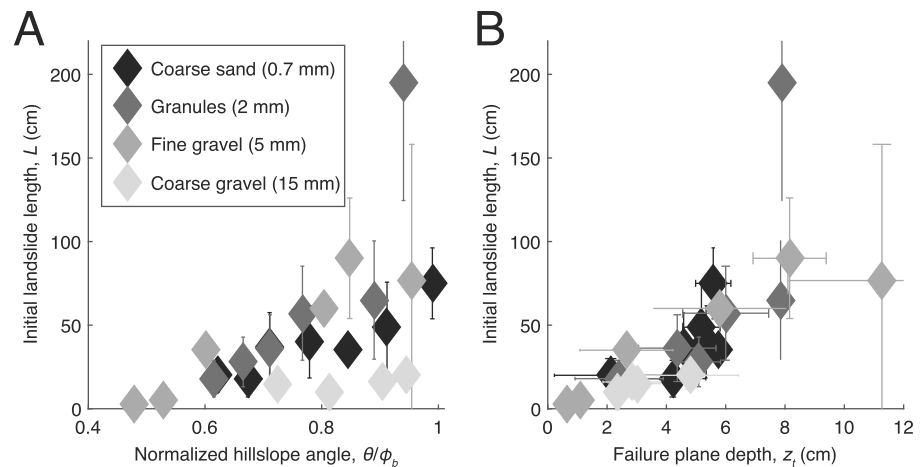
Figure 4. Initial landslide length, L, as a function of (a) hillslope angle, θ, relative to bulk friction angle, ϕ_b and (b) failure plane depth, z_t. The symbols represent average values for each experimental condition (grain size and slope). The symbols are shaded according to the grain size (sets 4 and 5 are combined). The error bars represent the standard deviation of lengths and failure plane depths for a given experimental condition.

4.2. Critical Saturation Level

The pore pressure measurements and visual estimates of flow depth provided two independent measures of the saturation level at the time of landslide initiation and are in agreement with each other (Table S1 and Figure 3). In general, the critical saturation levels, H_c, for all experiments exhibited the expected trend of decreasing with increasing hillslope angle, θ (Figure 3). This trend was most pronounced for the coarse sand experiments (Set 1), where there was a 40% reduction in the degree of saturation required to initiate failures from the saturated angle of repose to hillslope angles near the dry angle of repose. Experiment Sets 1, 2, and 4 had a total range of critical flow depths that spanned less than 3 cm. Relative to the total bed thickness, all experiments tended to fail when the water level was close to the bed surface. In fact, with the exception of experiments conducted very close to the dry bulk friction angle ($\theta > 0.9\phi_b$), failures were not initiated until the subsurface flow depth was within 1 cm of the bed surface. Even at hillslope angles approaching the dry bulk friction angle of each material, critical flow depths were never observed to be shallower than 50% of the bed thickness ($H_c/Z \geq 0.5$).

The critical saturation levels for all experiments were much higher than predicted by the infinite-slope stability model (equation (5)), which is in part due to boundary stresses. We included these boundary stresses by calculating the saturation level required to initiate the most susceptible prismatic landslide ($L = 4$ m and $W = 9.7$ cm) using equations (15) and (19). Because the lengths of the landslides are expected to be relatively long, including the effects of wall stress increases the predicted critical saturation level significantly (Figure 3). In contrast, because our flume was relatively narrow the predicted incremental increase in the critical saturation level associated with toe stress is comparatively small (Figure 3). Combined, boundary stresses result in an increase of 2 cm to 7 cm in saturation level required to initiate failure, depending on the experiment set (Figure 3). The stabilizing effect of boundary stresses is most significant in Experiment Sets 3 and 5 because those sediment beds were 2 to 3 times thicker than the other experiment sets. Surprisingly, though, even the 3-D model that accounts for frictional stresses on the boundaries of the expected landslide geometry ($L = 4$ m and $W = 9.7$ cm) predicts significantly lower critical saturation levels compared to all of our experimental observations.

4.3. Landslide Thickness

Within each experiment set we generally observed that the failure plane progressively deepened on steeper slopes (Figure 3 and Table S1). The shallowest failure plane depths were observed when the water surface was at or above the bed surface. For the gravel experiments that explored the supersaturated failure regimes (Sets 3 and 4), the minimum landslide thicknesses were between one and two grain diameters, and therefore scaled with grain size, consistent with the model of Takahashi (1978).

Within the subsaturated failure regime, the depth of failure planes did not scale with grain size, consistent with expectations. Despite an order of magnitude range in grain size between Experiment Sets 1, 2, and 3,
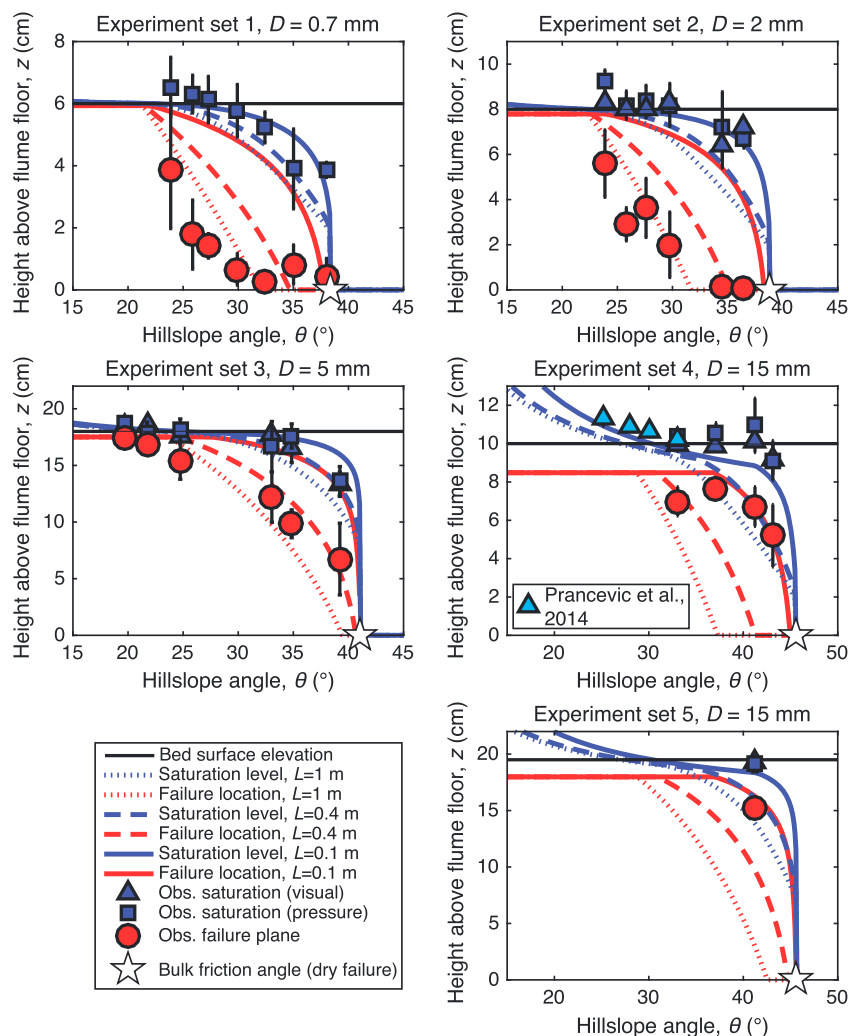
Figure 5. The same plots as shown in Figure 3 but with new model predictions made for the observed landslide geometries. The new model predictions show that landslide length is expected to affect both the saturation level required to initiate failures (blue lines) and the initial failure plane depth (red lines). Decreasing the landslide length to $L = 0.4$ m or $L = 0.1$ m yields a predicted increase in the stability of the sediment bed and improves the fit with our experimental results.

failure plane depths were roughly consistent for similar hillslope angles. For Sets 1 through 3, failure plane depths were roughly 1 cm thicker for every 2° of increased hillslope angle until the failure plane approached the rigid floor of the flume. Once the failure plane was close to the floor of the flume, which only occurred in Experiment Sets 1 and 2, then the failure plane depth was limited by the total bed thickness (Figure 3). Landslide thicknesses in Experiment Set 4, which used the coarsest gravel, did not vary with hillslope angle as much as the other sets, and failure planes were typically within several grain diameters of the bed surface.

The observed failure plane depths differ significantly from the infinite-slope stability model (equations (5) and (7)), which predicts that the failure plane abruptly shifts from the surface grain layer in the supersaturated failure regime ($H_c > Z$) to the deepest possible failure plane ($z_t = Z$) in the subsaturated regime ($H_c > Z$). Inclusion of wall and toe stresses can explain some of this difference. In general, resisting stresses at the walls and toe promote thinner landslides because earth pressure increases quadratically with depth (Figure 3; equations (8) and (9)). The predicted failure plane depths do not match all of our experimental data; the landslide thicknesses for the gravel is generally overpredicted compared to our observations, but the general trends are similar (Figure 3).
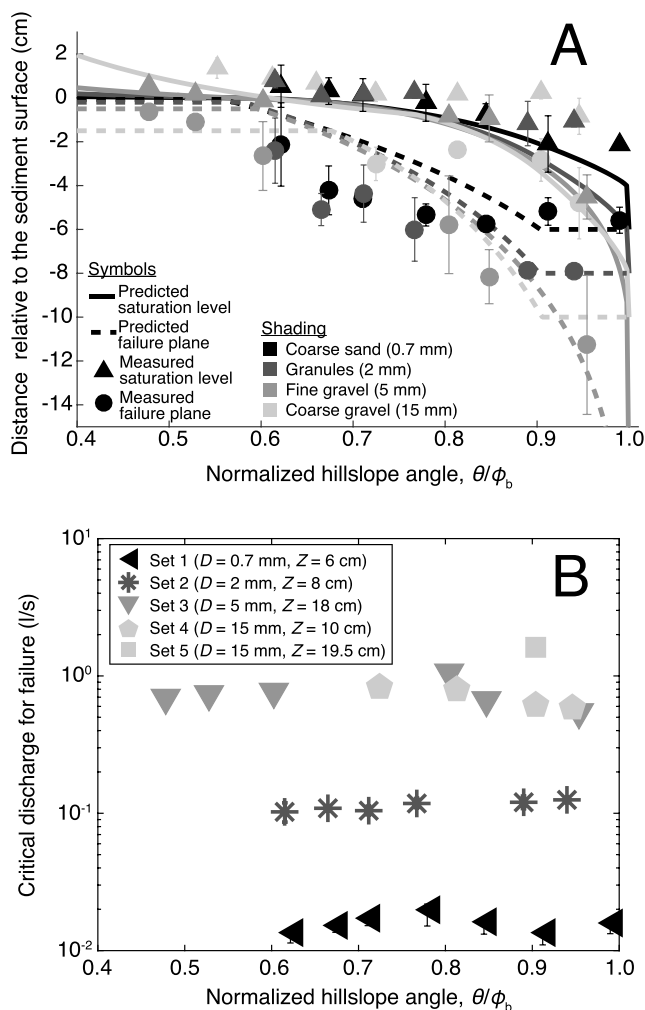
Figure 6. (a) Critical flow depth and landslide thickness measured relative to the bed surface and (b) critical discharge required to initiate landslides, as functions of relative hillslope angle for all experiments. In Figure 6a, all curves are model predictions that include boundary stresses for landslides of length $L = 0.4$ m. Solid lines indicate the predicted level of saturation below the bed surface required to initiate a landslide, and the dashed lines are the predicted landslide thicknesses. Triangles in Figure 6a represent the average of saturation depths measured visually and with the pressure sensors. Circles represent depths of failure planes. Data are differentiated by shading, corresponding to grain sizes. In Figure 6b, each symbol represents an average of the landslides observed at the same hillslope angle. Error bars represent the standard deviation of these discharge measurements, but most are smaller than the symbols.

4.4. Length and Width of Landslides

Boundary stresses are expected to have a greater stabilizing effect as landslides become shorter and narrower (equations (15) and (19)), suggesting that longer and wider landslides will be favored. For our experiments, this suggests that the most susceptible failure plane should have extended over the entire length of the uniform sediment bed (4 m) and across the entire width (9.7 cm). Consistent with this expectation, the width of all landslides spanned the entire width of the test section in our experiments, as observed in overhead video. However, landslides were not initiated along the entire length of the test section. Estimating the initial lengths of landslides was difficult, because they typically grew very quickly once initiated (Movies S2 to S5), but visual estimates from high-speed videos indicate that landslides began with lengths between 0.1 m and 1 m, with an average length of $L = 0.4$ m (Table S1). The variability of landslide length for a given experimental condition was large, but the data show a trend of increasing landslide length on steeper slopes (Figure 4a).

Using observed landslide lengths, we can refine our predictions for the critical saturation levels by substituting measured values of L into equations (15) and (19). For most of our experimental conditions, the predicted critical saturation levels associated with the range in observed landslide lengths bracket our experimental observations (Figure 5). However, for the coarse gravel (Set 4), the observed critical saturation levels for failure are slightly larger than model predictions.

4.5. Sediment Bed Thickness

Comparing the experimental landslides of Set 5 ($Z = 19.5$ cm) with those observed at the same hillslope angle in Set 4 ($Z = 10$ cm), both experiments required the same relative saturation level to initiate failure ($h_c/z \approx 1$), despite a twofold difference in bed thickness. Even with the thick sediment bed of Experiment Set 5, measured failure plane depths were less than three grain diameters on average ($z_t = 4.2 \pm 0.75$ cm), which is similar to the values measured for experiments at the same hillslope angle in Set 4 ($z_t = 3.3 \pm 1.03$ cm). This result is consistent with the stability model that includes the boundary stresses associated with the observed short landslides (Figure 5), which predicts that the failure plane depth in Experiment Set 5 is limited by strong wall and toe stresses rather than total bed thickness. Consequently, the model indicates that increasing the thickness of the sediment bed did not affect the depth of the failure plane.

In order to better compare our results between experiment sets with different bed thicknesses, we calculate the critical saturation level and landslide thickness with respect to the bed surface, rather than the base of the sediment bed ($H_c - Z$ and $L - Z$). Plotting this measure of critical saturation level and landslide thickness as a function of normalized hillslope angle collapses most of our experimental observations and model predictions to a single curve (Figure 6a). The data collapse 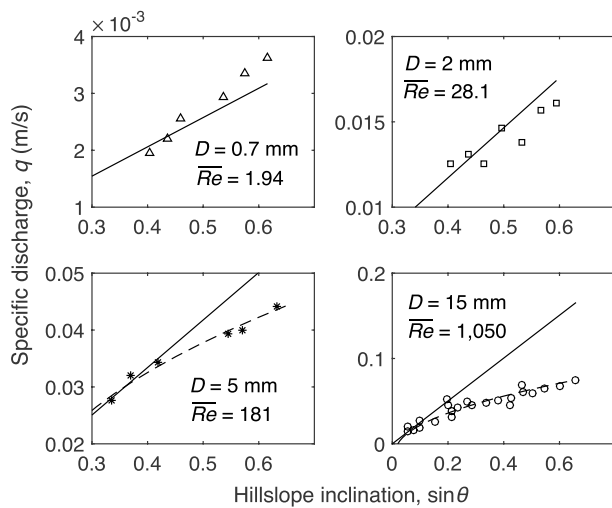is best at moderately steep slopes ($0.6 < \theta/\phi_b < 0.85$), corresponding to subsaturated landslides with depths smaller than the bed thickness. In cases where bed thickness is shallow relative to failure plane depth, landslide thickness can become limited by the total thickness of the bed on steep slopes ($z_{t,c} = Z$, as in Sets 1 and 2), which in turn forces the critical saturation level to be closer to the bed surface. On low-angle slopes where shallow landslides occur with some surface flow, grain diameter determines the depth of the failure plane and the critical saturation levels required to mobilize different landslide thicknesses diverge according to sediment size (Figure 6a).

4.6. Grain Size

Differences in sediment size resulted in a large range of subsurface Reynolds numbers, from the Darcian regime ($\overline{Re} = 1.94$) for the sand beds to the turbulent regime ($\overline{Re} \approx 1,000$) for the coarse gravel beds (Table 1).

Figure 7. Specific discharge as a function of $\sin\theta$ for each material. A good fit to a linear trend that crosses the origin, $q=0$ at $\sin\theta=0$ (shown in solid lines for each material), indicates that the subsurface flow is Darcian, while a curve that rolls over at steep slopes indicates non-Darcian flow (shown in dashed lines for the gravel materials).

In addition, specific discharge should scale linearly with the downslope component of gravity ($\sin\theta$) within the Darcian regime (Bear, 1972), as we observe with our sand bed experiments (Figure 7). In contrast, flow velocities through the gravel materials increase nonlinearly with hillslope angle (Figure 7) as expected for $Re > 10^2$ and non-Darcian flow (Bear, 1972). Despite orders-of-magnitude differences in subsurface specific discharge and Reynolds number, the saturation levels required to destabilize all grain sizes were relatively similar (Figure 6). Consequently, whether the subsurface flow is Darcian or not does not appear to affect saturation levels required to initiate landslides in our experiments.

5. Discussion
5.1. Enhanced Stability and Landslide Length
All of our experimental landslides required saturation levels that were higher than predicted by both the infinite-slope stability model and a stability model that considers resisting stresses acting on the walls and toe of a full-length landslide. Importantly, the enhanced stability of the experimental sediment beds for landsliding was apparent for different grain sizes that produced wide ranging subsurface flow Reynolds numbers and crossed the turbulent to Darcian subsurface flow regimes. The enhanced stability also occurred in experiment sets across both subsaturated to supersaturated regimes, which produced landslides with a wide range of failure plane depths. The length of the experimental landslides also deviated from the stability models that include boundary stresses, which predict that the longest possible failure plane ($L = 4$ m) should be least stable. Instead, we observed shorter landslide lengths, on average ($\bar{L} = 0.4$ m). The models better matched the saturation levels required to initiate failures when we prescribed the observed shorter landslide lengths in equations (15) and (19), rather than using the predicted longer values.

The enhanced stability of short landslides has been reported previously (Booth et al., 2014; Prancevic et al., 2014). Prancevic et al. (2014) noted that the infinite-slope model (without boundary stresses) matched their experimental observations only by using the dry bulk friction angle associated with landslides that are seven grain diameters long, which is ~10° larger than what was observed for a pile of thousands of grains. This issue was subsequently investigated by Booth et al. (2014), and they showed with experiments and numerical modeling that small groups of loose grains have higher effective bulk friction angles than large numbers of grains due to the increasing importance of "keystone" particles, which have anomalously high grain pocket friction angles. This effect is similar to the toe stresses as conceptualized in our equation (14), whereby the higher frictional resistance of the toe serves the role of the keystone particles and is able to support small patches of otherwise unstable grains upslope. For example, Figure 8 shows that the predicted critical avalanche angle ($\theta = \theta_c$) in equation (15) for the case of a dry granular slope ($H_c = 0$) matches well the observations from Prancevic et al. (2014) and Booth et al. (2014). These experimental observations and modeling results provide a consistent explanation for the increased saturation levels required to rupture short failure planes. However, it remains unclear why larger slides at the scale of the test section, which are predicted to be more prone to failure, did not occur at lower saturation levels.
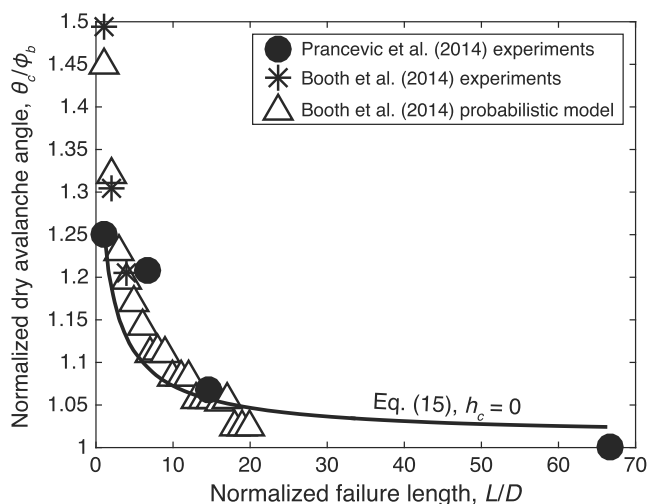
One possibility is that there is an optimal length-to-width ratio for landslides, and therefore, longer slides did not occur in our experiments because of the relatively narrow width. In our experiments, we observed that landslide lengths were mostly of the same order of magnitude as the landslide width at the time of initiation (Figure 4). Observations of landslide initiation in natural settings are rare, but several studies have estimated the geometry of landslide source areas from landslide scars, and they find similar length-to-width ratios of $1 < L/W < 10$ (Dai & Lee, 2002; Reneau & Dietrich, 1987; Taylor et al., 2015).

Figure 8. Dry avalanche angle relative to bulk friction angle as a function of landslide length for two independent sets of physical experiments (circles and asterisks), one set of numerical probabilistic experiments (triangles), and the predicted dry avalanche angle predicted by equation (15), which includes the stabilizing stresses due to friction along the walls and toe of the landslide.

A possible explanation is that this range in L/W reflects the geometry of convergent hollows; however, initial landslide lengths are often much shorter than the limit imposed by topography (e.g., Montgomery et al., 2009; Reneau & Dietrich, 1987). Using a slope stability model with wall and toe stresses, Milledge et al. (2014) predict a similar optimal length-to-width ratio ($L/W \approx 2$) for landslides, but only if the total landslide volume is held fixed. However, in our experiments longer landslides also had larger volumes, and therefore, longer landslides still should have been the least stable according to the model of Milledge et al. (2014).

The slope stability model presented here explicitly assumes that hydrologic and granular conditions are uniform along the length (and width and depth) of the test section, and the mechanism promoting short landslides may be related to heterogeneities in sediment properties. Although we attempted to construct the sediment bed in a uniform manner, natural granular material is inherently variable at the grain scale. This variability produces heterogeneities in the local friction angle, permeability, and porosity, as evident by standard deviations on the order of 10% in pore pressure measurements (Table S1) and 2% for bulk friction angle measurements (Table 2). The importance of this variability is likely dependent on the scale of the landslide. For example, shorter patches of sediment have wider distributions of bulk friction angles (Booth et al., 2014; Prancevic et al., 2014). As sediment beds get longer, they become increasingly likely to contain small patches of unstable grains, leading to lower bulk friction angles and narrower distributions. However, the probability of having patches with anomalously high stability also increases, potentially stabilizing the sediment with respect to long landslides. These anomalies in local friction angle may favor short landslides, despite higher sensitivity to toe stresses for short landslides (equation (14)). A preference for short landslides has also been observed in dry granular avalanches (Bretz et al., 1992; Cantelaube et al., 1995), which is consistent with an explanation rooted in granular mechanics.

In our experiments, the competition between sediment heterogeneity over short length scales and reduced relative contribution of toe stress for long landslides may result in a preferred failure plane length. This could explain why landslides tended to lengthen on steeper slopes, where deeper failure planes are favored (Figure 4b). Thicker landslides require a greater length of unstable mass to overcome larger toe resistance.

5.2. Stability and Reynolds Number

In some derivations of the infinite-slope stability model, researchers have specified the requirement that the subsurface flow is within the Darcy regime (Bear, 1972; Iverson & Major, 1986), although other derivations do not specify this requirement (Lambe & Whitman, 1969; Takahashi, 1978), including ours (equation (4)). We argue that as long as the fluid is not accelerating after averaging over the relevant volume (the landslide block, in this case), the seepage stress must balance the gravitational driving stress, and therefore equation (4) should be valid even for non-Darcian flow. Our experimental observations, which span a wide range in Re for different granular materials, are consistent with this interpretation and show similar agreement with model predictions in both the Darcian and non-Darcian flow regimes (Figure 6a). This includes the fine gravel which had $Re > 10^2$ and flow velocities that clearly diverged from Darcian (Figure 7).

Although landslides in the experiments with the coarsest gravel required the highest saturation levels, we do not interpret this as a Reynolds-number effect. Instead, the tendency for the coarsest material to be more stable than the rest of the tested materials may be a result of the small ratio of flume width to grain size ($W/D = 6.5$). This ratio is within the regime where force chains between particles can bridge the width of the test section to provide an additional stabilizing force (Andrade & Avila, 2012; Booth et al., 2014; Peters et al., 2005; Zimmermann et al., 2010). Consequently, the stability of coarse sediment in these experiments is likely underestimated because our model does not account for stabilizing force chains.

5.3. Application to Natural Landscapes

Enhanced stability of hillslopes and channel beds to landsliding has been observed previously at both the hillslope and landscape scale (Berti & Simoni, 2005; Montgomery & Dietrich, 1994; Montgomery et al. 2009; Stock & Bellugi, 2011) but is often attributed to root strength or complex seepage paths. While these effects can stabilize soil, our results show that enhanced stability is expected even in their absence due to frictional stresses at the boundaries of landslides and the tendency for failures to be localized. Our results indicate that the critical saturation level can be calculated if landslide geometries are known, but we do not currently have the ability to predict landslide size. Previous efforts to predict landslide size and location rely on finding minimum-strength patches using the slope stability model that includes wall and toe stresses (Bellugi, Milledge, Dietrich, Perron, et al., 2015; Dietrich et al., 2007; Milledge et al., 2014). However, our experimental results indicate that if the landslide volume is unknown, the model fails to predict the landslide length,

even if the landslide width is well constrained. In addition, we observe that landslide length increases on steeper slopes, and while we propose that this lengthening is caused by higher toe friction acting on deeper failure planes, this behavior is not captured by model predictions. We interpret the observed short landslide lengths to result from spatial heterogeneities in frictional resistance and driving stress, but we lack methods to characterize this heterogeneity.

In situations where no constraints on landslide size are available, our results indicate that assuming fully saturated conditions at failure will yield more accurate predictions of the critical saturation level than using an infinite-slope stability model (Figure 3). Despite the wide range of bed angles, grain sizes, and sediment bed thicknesses tested in our study, 24 of 28 experimental conditions produced failure events when the water surface was very close to the sediment bed surface $H_c/Z = 1 \pm 0.15$ (Figure 6a). In all of our experiment sets there was a decrease in the saturation level required to initiate landslides on steeper slopes, but the trend is much less pronounced than that predicted by the infinite-slope model. Moreover, experiments with steeper slopes had faster seepage velocities (Figure 7), and consequently, all experiments required similar water discharges to initiate landslides within an experiment set (Figure 6b and Table S1). This suggests that landsliding might depend more on hydrological factors (contributing drainage area, soil thickness, and hydraulic conductivity) and less on hillslope angle, as compared with the infinite-slope stability model. For example, changing sediment size (and the associated change in hydraulic conductivity) or bed thickness has a larger effect on the critical discharge required for failure than changes in the hillslope angle (Figure 6b and Table S1). Therefore, in landscapes that are eroded predominantly by landslides, changes in erosion rate will not necessarily be accommodated by changes in hillslope angle. This is consistent with field observations that show that hillslope gradients are insensitive to changes in erosion rate in landscapes where storm-induced landslides are the dominant erosion mechanism (e.g., Clarke & Burbank, 2010; DiBiase et al., 2012; Larsen & Montgomery, 2012).

Previous studies have proposed that thicker hillslope soils are less stable than thin ones, because root strength tends to decrease with depth (Dietrich & Dunne, 1978; Gabet & Dunne, 2002; Reneau & Dietrich, 1987). In contrast, our experiments reveal that thicker beds of cohesionless sediment can require substantially higher subsurface dicharges for failure to occur (Experiment Set 4 versus 5). This is partly because thick soils are held in place by strong wall and toe stresses, forcing the failure plane and water level to be close to the surface. On hillslopes with thinner soils, relative to landslide length and width, boundary stresses become less important, and previous numerical analyses suggest that the 3-D stability model nearly converges to the 1-D infinite-slope model when the length-to-thickness ratio exceeds $L/z_t > 25$ (Milledge et al., 2012). For comparison, the length-to-thickness ratios examined in these experiments were all smaller than this critical ratio ($3.0 \leq L/z_t \leq 25$), as are most natural shallow landslides (Larsen et al., 2010), suggesting that boundary stresses are important in most cases.

Consistent with theoretical predictions (Takahashi, 1978), the shallowest failure planes in our experiments were observed at low hillslope angles within the supersaturated failure regime and were set by the typical grain diameter of the sediment (Experiment Sets 3 and 4). This finding indicates that landslide initiation in the supersaturated regime is very sensitive to sediment size, particularly where cohesion from plant roots is negligible. For example, in steep landscapes, wildfires can cause the release of sandy sediment that mantles otherwise bouldery channel beds (Lamb et al., 2011), and these channel beds subsequently become the initiation sites for shallow landslides when surface runoff is present (Kean et al., 2011). These channel experience surface flow on an annual basis, but landslides and debris flows are far more common after wildfires load the channels with sand and pebbles (Cannon, 2001; Lamb et al., 2011). The grain size dependence of supersaturated failures could thus help explain the increased debris flow activity following wildfires.

6. Conclusions

We conducted experimental tests of the saturation levels required to initiate landslides in sloping sediment beds experiencing steady, slope-parallel seepage in an effort to test 1-D (infinite slope) and 3-D (including wall and toe stresses) stability models. For all tested sediment sizes and at all hillslope angles, the sediment beds were more stable than predicted by both of these models. Although the boundary stress model (3-D) predicts that the largest possible landslides should occur most easily, the experimental landslides typically spanned only a few decimeters in length. The increased contribution of toe stresses for the observed short landslides accounts for the increased saturation levels required for landslide initiation. The preference for short

landslides may result from local heterogeneities in friction angle and seepage stress that are not captured in slope stability models. We observe that landslides are longer on steeper slopes, but on average they have similar length-to-width ratios of natural landslide scars, suggesting that there may be a common mechanism giving rise to landslides with a certain aspect ratio.

Although our experiments probed a wide parameter space for sediment size, hillslope angle, and bed thickness, landslides were only initiated when the sediment bed was very close to full water saturation in nearly all experiments. Model predictions indicate that the tendency for failure at saturation occurs because frictional stresses acting on the wall and toe of the landslides inhibit deep failure planes, pushing the failure plane and the critical saturation level closer to the land surface. We found that the slight reduction in the saturation level required to initiate landslides on steep slopes was offset by faster seepage velocities, such that sediment beds at all hillslope angles required similar subsurface discharges to fail. By comparing discharges required to initiate landslides between experiment sets, we find that grain size and bed thickness play a much more important role than hillslope angle in determining critical discharges.

In most of our experiments, landslide thickness was not set by the total bed thickness, but was instead determined by a balance between boundary friction and driving stresses, both of which increase with depth. We observe that landslide thickness increases on steeper slopes in a trend that is consistent with our theoretical expectations. Within the supersaturated regime on low bed slopes, failure plane depths in cohesionless soils are approximately equal to one or two sediment diameters. Consequently, the depth of surface flow required to initiate failure scales with sediment size, potentially explaining the increased occurrence of debris flows following inputs of relatively fine sediment to otherwise coarse channel beds.

References

Andrade, J. E., & Avila, C. F. (2012). Granular element method (GEM): Linking inter-particle forces with macroscopic loading. *Granular Matter*, *14*(1), 51–61. https://doi.org/10.1007/s10035-011-0298-8

Bear, J. (1972). *Dynamics of fluids in porous media*. New York, NY: Elsevier.

Bellugi, D., Milledge, D. G., Dietrich, W. E., McKean, J. A., Perron, J. T., Sudderth, E. B., & Kazian, B. (2015). A spectral clustering search algorithm for predicting shallow landslide size and location. *Journal of Geophysical Research: Earth Surface*, *120*, 300–324. https://doi.org/10.1002/2014JF003137

Bellugi, D., Milledge, D. G., Dietrich, W. E., Perron, J. T., & McKean, J. (2015). Predicting shallow landslide size and location across a natural landscape: Application of a spectral clustering search algorithm. *Journal of Geophysical Research: Earth Surface*, *120*, 2552–2585. https://doi.org/10.1002/2015JF003520

Berti, M., & Simoni, A. (2005). Experimental evidences and numerical modelling of debris flow initiated by channel runoff. *Landslides*, *2*(3), 171–182. https://doi.org/10.1007/s10346-005-0062-4

Booth, A. M., Hurley, R., Lamb, M. P., & Andrade, J. E. (2014). Force chains as the link between particle and bulk friction angles in granular material. *Geophysical Research Letters*, *41*, 8862–8869. https://doi.org/10.1002/2014GL061981

Bretz, M., Cunningham, J. B., Kurczynski, P. L., & Nori, F. (1992). Imaging of avalanches in granular materials. *Physical Review Letters*, *69*, 2431–2434. https://doi.org/10.1103/PhysRevLett.69.2431

Burroughs, E. R. (1984). Landslide hazard rating for portions of the Oregon Coast range. In *Proceedings of the Symposium on Effects of Forest Land use on Erosion and Slope Stability* (pp. 265–274).

Cannon, S. H. (2001). Debris-flow generation from recently burned watersheds. *Environmental and Engineering Geoscience*, *7*(4), 321–341. https://doi.org/10.2113/gseegeosci.7.4.321

Cantelaube, F., Limon-Duparcmeur, Y., Bideau, D., & Ristow, G. H. (1995). Geometrical analysis of avalanches in a 2D drum. *Journal de Physique I*, *5*(5), 581–596. https://doi.org/10.1051/jp1:1995107

Carson, M. A. (1977). Angles of repose, angles of shearing resistance and angles of talus slopes. *Earth Surface Processes and Landforms*, *2*(4), 363–380. https://doi.org/10.1002/esp.3290020408

Chaudhry, M. H. (2008). *Open-channel flow*. New York, NY: Springer US.

Clarke, B. A., & Burbank, D. W. (2010). Bedrock fracturing, threshold hillslopes, and limits to the magnitude of bedrock landslides. *Earth and Planetary Science Letters*, *297*(3), 577–586. https://doi.org/10.1016/j.epsl.2010.07.011

Dai, F. C., & Lee, C. F (2002). Landslide characteristics and slope instability modeling using GIS, Lantau Island, Hong Kong. *Geomorphology*, *42*(3), 213–228. https://doi.org/10.1016/S0169-555X(01)00087-3

DiBiase, R. A., Heimsath, A. M., & Whipple, K. X. (2012). Hillslope response to tectonic forcing in threshold landscapes. *Earth Surface Processes and Landforms*, *37*(8), 855–865. https://doi.org/10.1002/esp.3205

Dietrich, W. E., & Dunne, T. (1978). Sediment budget for a small catchment in a mountainous terrain. *Zeitschrift fü Geomorphologie*, *29*, 191–206.

Dietrich, W. E., McKean, J., Bellugi, D., & Perron, T. (2007). The prediction of shallow landslide location and size using a multidimensional landslide analysis in a digital terrain model. In C. L. Chen & J. J. Major (Eds.), *Debris-Flow Hazards Mitigation: Mechanics, Prediction, and Assessment: Proceedings 4th International Dfhm Conference* (pp. 1–12). Chengdu, China.

Eckersley, D. (1990). Instrumented laboratory flowslides. *Géotechnique*, *40*(3), 489–502. https://doi.org/10.1680/geot.1990.40.3.489

Gabet, E. J., & Dunne, T. (2002). Landslides on coastal sage-scrub and grassland hillslopes in a severe El Niño winter: The effects of vegetation conversion on sediment delivery. *Geological Society of America Bulletin*, *114*(8), 983–990. https://doi.org/10.1130/0016-7606(2002)114<0983:LOCSSA>2.0.CO;2

Haefeli, R. (1948). The stability of slopes acted upon by parallel seepage. In *Proceedings of the 2nd International Conference on Soil Mechanics and Foundation Engineering*, Rotterdam (pp. 57–62).

Iverson, R. M., Reid, M. E., Iverson, N. R., LaHusen, R. G., Logan, M., Mann, J. E., & Brien, D. L. (2000). Acute sensitivity of landslide rates to initial soil porosity. *Science*, *290*(5491), 513–516. https://doi.org/10.1126/science.290.5491.513

Iverson, R. M., Reid, M. E., & LaHusen, R. G. (1997). Debris-flow mobilization from landslides. *Annual Review of Earth and Planetary Sciences*, *25*, 85–138.

Iverson, R. M., Logan, M., & Denlinger, R. P. (2004). Granular avalanches across irregular three-dimensional terrain: 2. Experimental tests. *Journal of Geophysical Research*, *109*, F01015. https://doi.org/10.1029/2003JF000084

Iverson, R. M., & Major, J. J. (1986). Groundwater seepage vectors and the potential for hillslope failure and debris flow mobilization. *Water Resources Research*, *22*(11), 1543–1548. https://doi.org/10.1029/WR022i011p01543

Jaky, J. (1944). The coefficient of earth pressure at rest. *Journal of Union of Estonian Architects*, *78*(22), 355–358.

Kean, J. W., Staley, D. M., & Cannon, S. H. (2011). In situ measurements of post-fire debris flows in Southern California: Comparisons of the timing and magnitude of 24 debris-flow events with rainfall and soil moisture conditions. *Journal of Geophysical Research*, *116*, F04019. https://doi.org/10.1029/2011JF002005

Lamb, M. P., Scheingross, J. S., Amidon, W. H., Swanson, E., & Limaye, A. (2011). A model for fire-induced sediment yield by dry ravel in steep landscapes. *Journal of Geophysical Research*, *116*, F03006. https://doi.org/10.1029/2010JF001878

Lambe, T. W., & Whitman, R. V. (1969). *Soil mechanics*. New York, NY: John Wiley.

Larsen, I. J., & Montgomery, D. R. (2012). Landslide erosion coupled to tectonics and river incision. *Nature Geoscience*, *5*(7), 468–473.

Larsen, I. J., Montgomery, D. R., & Korup, O. (2010). Landslide erosion controlled by hillslope material. *Nature Geoscience*, *3*(4), 247–251.

Lu, N., & Likos, W. J. (2004). *Unsaturated soil mechanics*. Hoboken, NJ: John Wiley.

Lu, N., & Godt, J. (2008). Infinite slope stability under steady unsaturated seepage conditions. *Water Resources Research*, *44*, W11404. https://doi.org/10.1029/2008WR006976

Milledge, D. G., Griffiths, D. V., Lane, S. N., & Warburton, J. (2012). Limits on the validity of infinite length assumptions for modelling shallow landslides. *Earth Surface Processes and Landforms*, *37*(11), 1158–1166. https://doi.org/10.1002/esp.3235

Milledge, D. G., Bellugi, D., McKean, J. A., Densmore, A. L., & Dietrich, W. E. (2014). A multidimensional stability model for predicting shallow landslide size and shape across landscapes. *Journal of Geophysical Research: Earth Surface*, *119*, 2481–2504. https://doi.org/10.1002/2014JF003135

Montgomery, D. R., & Dietrich, W. E. (1994). A physically based model for the topographic control on shallow landsliding. *Water Resources Research*, *30*(4), 1153–1171. https://doi.org/10.1029/93WR02979

Montgomery, D. R., Schmidt, K. M., Dietrich, W. E., & McKean, J. (2009). Instrumental record of debris flow initiation during natural rainfall: Implications for modeling slope stability. *Journal of Geophysical Research*, *114*, F01031. https://doi.org/10.1029/2008JF001078

Moriwaki, H. (1993). Behavior of pore-water pressure at slope failure. In S. Novosad, & P. Wagner (Eds.), *Proceedings of the Seventh International Conference and Field Workshop on Landslides in Czech and Slovak Republics* (pp. 263–268). Rotterdam.

Moriwaki, H., Inokuchi, T., Hattanji, T., Sassa, K., Ochiai, H., & Wang, G. (2004). Failure processes in a full-scale landslide experiment using a rainfall simulator. *Landslides*, *1*(4), 277–288. https://doi.org/10.1007/s10346-004-0034-0

Okura, Y., Kitahara, H., Ochiai, H., Sammori, T., & Kawanami, A. (2002). Landslide fluidization process by flume experiments. *Engineering Geology*, *66*(1), 65–78. https://doi.org/10.1016/S0013-7952(02)00032-7

Peters, J. F., Muthuswamy, M., Wibowo, J., & Tordesillas, A. (2005). Characterization of force chains in granular material. *Physical Review E*, *72*(041307), 1–8. https://doi.org/10.1103/PhysRevE.72.041307

Petley, D. (2012). Global patterns of loss of life from landslides. *Geology*, *40*(10), 927–930. https://doi.org/10.1130/G33217.1

Prancevic, J. P., Lamb, M. P., & Fuller, B. M. (2014). Incipient sediment motion across the river to debris-flow transition. *Geology*, *42*(3), 191–194. https://doi.org/10.1130/G34927.1

Reid, M. E., Christian, S. B., Brien, D. L., & Henderson, S. T. (2015). Scoops3d: Software to analyze 3D slope stability throughout a digital landscape (*Techniques and Methods*). Reston, VA: U.S. Geological Survey. https://doi.org/10.3133/tm14A1

Reid, M. E., LaHusen, R. G., & Iverson, R. M. (1997). Debris-flow initiation experiments using diverse hydrologic triggers. In C. L. Chen (Ed.), *Debris-flow Hazards Mitigation: Mechanics, Prediction, and Assessment: Proceedings 1st International dfhm Conference* (pp. 1–11). San Francisco, CA.

Reneau, S. L., & Dietrich, W. E. (1987). Size and location of colluvial landslides in a steep forested landscape. In R. L. Beschta, T. Blinn, G. E. Grant, F. J. Swanson, & G. G. Ice (Eds.), *Erosion and sedimentation in the Pacific rim* (pp. 39–48). Corvallis, Oregon: International Association of Hydrological Sciences.

Rickenmann, D., & Zimmermann, M. (1993). The 1987 debris flows in switzerland: Documentation and analysis. *Geomorphology*, *8*(2), 175–189. https://doi.org/10.1016/0169-555X(93)90036-2

Schmidt, K. M., Roering, J. J., Stock, J. D., Dietrich, W. E., Montgomery, D. R., & Schaub, T. (2001). The variability of root cohesion as an influence on shallow landslide susceptibility in the Oregon Coast range. *Canadian Geotechnical Journal*, *38*(5), 995–1024. https://doi.org/10.1139/t01-031

Skempton, A. W., & DeLory, F. A. (1957). Stability of natural slopes in London clay. In *Proceedings of the 4th International Conference on Soil Mechanics* (Vol. 2, pp. 378–381). London

Stark, T. D., & Eid, H. T. (1998). Performance of three-dimensional slope stability methods in practice. *Journal of Geotechnical and Geoenvironmental Engineering*, *124*(11), 1049–1060.

Stock, J. D., & Bellugi, D. (2011). An empirical method to forecast the effect of storm intensity on shallow landslide abundance. In *5th International Conference on Debris-Flow Hazards Mitigation: Mechanics, Prediction, and Assessment*. https://doi.org/10.4408/IJEGE.2011-03.B-110

Stock, J. D., & Dietrich, W. E. (2006). Erosion of steepland valleys by debris flows. *Geological Society of America Bulletin*, *118*(9-10), 1125–1148. https://doi.org/10.1130/B25902.1

Takahashi, T. (1978). Mechanical characteristics of debris flow. *Journal of the Hydraulics Division-ASCE*, *104*(HY8), 1153–1169.

Taylor, D. W. (1948). *Fundamentals of soil mechanics*. New York, NY: John Wiley.

Taylor, F. E., Malamud, B. D., & Witt, A. (2015). What shape is a landslide? Statistical patterns in landslide length to width ratio. In *Egu General Assembly Conference Abstracts* (Vol. 17, 10191 pp.).

United States Geological Survey (2005). Landslide hazards—A national threat. *United States Geological Survey Fact Sheet*, *2005-3156*.

von Ruette, J., Lehmann, P., & Or, D. (2013). Rainfall-triggered shallow landslides at catchment scale: Threshold mechanics-based modeling for abruptness and localization. *Water Resources Research*, *49*, 6266–6285. https://doi.org/10.1002/wrcr.20418

von Ruette, J., Lehmann, P., & Or, D. (2016). Linking rainfall-induced landslides with predictions of debris flow runout distances. *Landslides*, *13*(5), 1097–1107. https://doi.org/10.1007/s10346-015-0621-2

Waldron, L. J., & Dakessian, S. (1981). Soil reinforcement by roots: Calculation of increased soil shear resistance from root properties. *Soil Science*, *132*(6), 427–435.

Wang, G., & Sassa, K. (2003). Pore-pressure generation and movement of rainfall-induced landslides: Effects of grain size and fine-particle content. *Engineering Geology*, *69*(1), 109–125. https://doi.org/10.1016/S0013-7952(02)00268-5

Yagi, N., & Yatabe, R. (1987). Prediction method of slope failure in sandy soil due to rainfall. In *Proceedings of the 8th Asian Regional Conference on Soil Mechanics and Foundation Engineering* (pp. 217–220). Kyoto.

Zeng, Z., & Grigg, R. (2006). A criterion for non-Darcy flow in porous media. *Transport in Porous Media*, *63*(1), 57–69. https://doi.org/10.1007/s11242-005-2720-3

Zimmermann, A., Church, M., & Hassan, M. A. (2010). Step-pool stability: Testing the jammed state hypothesis. *Journal of Geophysical Research*, *115*, F02008. https://doi.org/10.1029/2009JF001365